

1

## REVISION 1

# 2 Chlorite topography and dissolution of the interlayer studied with 3 Atomic Force Microscopy.

4

5 Salvatore A. Gazzè<sup>1</sup>, Andrew G. Stack<sup>2</sup>, K. Vala Ragnarsdottir<sup>3</sup> and Terence J. McMaster<sup>1,4</sup>

6

7 <sup>1</sup> School of Physics, University of Bristol, Bristol, UK.

8 <sup>2</sup> Chemical Sciences Division, Oak Ridge National Laboratory, Oak Ridge, USA.

9 <sup>3</sup> Institute of Earth Sciences, School of Engineering and Natural Sciences, University of  
10 Iceland, Reykjavik, Iceland.

11 <sup>4</sup> Bristol Centre for Functional Nanomaterials, University of Bristol, Bristol, UK

12

### 13 Abstract

14 Chlorite has a structure composed of a combination of two distinct layers, the tetrahedral-  
15 octahedral-tetrahedral (TOT) and the interlayer (i.e. the octahedral layer between TOT layers).  
16 In this study, the morphology and dissolution of chlorite in pure water has been visualized  
17 using Atomic Force Microscopy. Upon cleavage, the TOT layer shows atomically flat  
18 terraces and steps, while the interlayer presents strips and voids. In pure water, dissolution

1

19 channels and equilateral, mono-oriented triangular etch pits form in the interlayer and lead to  
20 progressively increased solubilisation. Dissolution channels are proposed to originate from  
21 structural defects, while a conceptual model is discussed to explain the presence of triangular  
22 etch pits. In this model, their formation is driven by the different reactivity of the two  
23 octahedral configurations along the etch pits. It is not currently known which of these is the  
24 most stable configuration, however we propose arguments that point towards a specific  
25 orientation. The conceptual model is supported by experimental data and is potentially  
26 applicable to all mineral structures constituted by continuous octahedral layers.

27

## 28 **1. Introduction**

29 Chlorite, a mineral common in sedimentary and metamorphic rocks (Hamer et al. 2003) as  
30 well in soils (Glowa et al. 2003), is a 2:1:1 phyllosilicate that consists of alternating 2:1  
31 layers and octahedral interlayer sheets, Fig. 1, with a unit cell c-dimension of 14 Å (Bailey  
32 1988). The 2:1 layer is named the TOT layer for its tetrahedral-octahedral-tetrahedral  
33 structure; it is also referred to as the talc-like layer because of its structural similarity with the  
34 talc mineral. This layer presents an excess of negative charge: unlike other 2:1 phyllosilicates  
35 in which the negative charge is neutralized by positive cations, in chlorite the same function  
36 is accomplished by a positively-charged hydroxyl interlayer (Bailey 1988), also referred to as  
37 the brucite-like layer.

38 Atomic Force Microscopy (AFM) (Binnig et al. 1986) has been used extensively to probe  
39 phyllosilicate nano-structure and weathering, as it has the advantage of being able to image  
40 and follow alteration of mineral topography in real-time under ambient and elevated

41 temperature/pressure conditions (e.g. Aldushin et al. 2006; Sánchez-Pastor et al. 2010;  
42 Kuwahara 2001; Bickmore et al. 2001). While bulk dissolution studies provide information  
43 on reaction rates and products, visualizing the three-dimensional topography at the nanoscale  
44 AFM can add important, complementary knowledge such as: the role of surface  
45 heterogeneity, the mechanisms of surface complexation and dissolution, and the detection of  
46 secondary phase formation (Maurice et al. 1996).

47 In this regard, chlorite represents an interesting substrate for AFM studies due to its  
48 composite TOT plus interlayer structure, which presents different surface topographies and  
49 dissolution processes of the two layers. As already shown by Antognozzi et al. (2006) and  
50 Valdrè et al. (2009), the two layers can be easily recognized with AFM due to their different  
51 thickness (10 Å in the TOT and 4 Å in the interlayer, Fig. 1) and their different surface  
52 potentials (TOT is negatively charged and the interlayer is positively charged). The latter  
53 property is revealed by the AFM cantilever oscillation phase signal in “Tapping” mode,  
54 which is sensitive to material composition and properties (Schmitz et al. 1997). In this mode,  
55 the oscillations of the tip are affected by differences in the surface potential of the two  
56 chlorite layers and lead to a phase lag.

57 The only AFM study on chlorite dissolution that exists to date has shown that the interlayer  
58 dissolves faster than the TOT component, and these conclusions were based on visual  
59 observations of grain edge retreat (Brandt et al. 2003). The reason for this different reactivity  
60 lies in the different structures of the two layers: the TOT layer is similar in structure to  
61 common 2:1 phyllosilicates, such as muscovite and talc, which have dissolution rates of order  
62  $10^{-13} \text{ mol m}^{-2} \text{ s}^{-1}$  at near neutral pH (White and Brantley 1995). In contrast, the interlayer has

63 a structure similar to the brucite mineral, which has a dissolution rate about 7 orders of  
64 magnitude faster than the 2:1 phyllosilicates (White and Brantley 1995).

65 The analysis of 2:1 phyllosilicates dissolution by means of AFM is non-trivial due to their  
66 resistance to dissolution; a pre-treatment of the surfaces and extreme weathering conditions,  
67 uncommon in soils and rocks, is sometimes required to observe weathering in the time-frame  
68 of a typical AFM experiment (Bickmore et al. 2001; Rufe and Hochella 1999). Brandt et al.  
69 (2003) pre-conditioned the chlorite grains at pH 2 for several months before the AFM  
70 analysis took place; chlorite grains were also obtained through mechanical grinding, which  
71 introduced cracks and other surface defects. Although the TOT and interlayer edge retreats  
72 were successfully observed, these pre-treatments precluded the evaluation of chlorite  
73 structural alterations from its pristine state. Unlike TOT-structured minerals, brucite can be  
74 easily studied with AFM in mild weathering conditions because of its higher dissolution rate,  
75 as in Kudoh et al. (2006). In their study, brucite formed mono-oriented triangular etch pits  
76 while dissolving, a phenomenon attributed to the three-fold axis of symmetry normal to the  
77 (001) surface.

78 In this study, our aim is to further characterize chlorite structure and dissolution in the near-  
79 pristine state by AFM imaging of surfaces of the mineral in pure water at near-neutral pH;  
80 and by examining its reactivity with a special focus on the interlayer component, the most  
81 prone to dissolution in mild conditions.

82

## 83 **2. Materials and Methods**

84 **2.1 Preparation of the chlorite flakes.** The empirical formula of the chlorite sample was  
85 determined with Electron Probe Micro Analysis (EPMA), and recorded as:  $(\text{Mg}_{4.90} \text{Fe}_{0.31}$   
86  $\text{Ti}_{0.001} \text{Mn}_{0.005} \text{Al}_{0.74}) (\text{Si}_{3.34}, \text{Al}_{0.66}) \text{O}_{10} (\text{OH})_8$ . Mineral flakes, with thicknesses of less than 1  
87 mm and areas around  $1 \text{ cm}^2$ , were attached to PTFE disks with a few drops of EPO-TEK  
88 302-3M (Epoxy Technology, Billerica, MA 01821, U.S.A), a two-component epoxy highly  
89 resistant to water, solvents and acids. After the epoxy resin was cured, samples were cleaved  
90 by removing the external mineral (001) surface with adhesive tape (Scotch-brand, 3M) gently  
91 adhered to the (001) surface.

92 **2.2 AFM imaging.** A Bruker Multimode AFM (Bruker, Santa Barbara, CA, USA) was used,  
93 equipped with a J scanner, a NanoScope IIIA controller and an Extender Module. The  
94 adopted cantilevers were V-shaped (Bruker, Santa Barbara, CA, USA), with a nominal  
95 resonance frequency of 56 kHz and a nominal spring constant of  $0.24 \text{ N m}^{-1}$ . Chlorite  
96 imaging and dissolution studies were undertaken in a batch system under  $18.2 \text{ M}\Omega\text{-cm}$  ultra-  
97 pure water (Fluka, UK) using a Veeco fluid cell and at a scan rate of 1 Hz. Observations were  
98 carried out in Tapping Mode (TM), except where specified. Two different AFM signals were  
99 recorded, the height and the phase lag signal. The first was used to visualize the topography  
100 of the chlorite surface, while the second to distinguish the TOT layer and the interlayer. In  
101 this work images constituted by the phase lag signals are labelled as “Phase image”. Off-line  
102 processing consisted of low-order flattening, plane fitting and image analysis subroutines of  
103 the Nanoscope 5.30r1 software suite (Bruker, Santa Barbara, CA, USA) and WSxM 5.0  
104 (Horcas et al. 2007).

105 **2.3 Dissolution Kinetics.** The formula from Rufe and Hochella (1999) was adopted to  
106 calculate the dissolution kinetics:  $\text{rate} = (\Delta V/V_m)/(SA t)$  (1), where  $\Delta V$  is the dissolved mineral  
107 volume between two consecutive AFM images,  $V_m$  is the molar volume of the mineral,  $SA$  is  
108 the total mineral area considered and  $t$  is the time. The volume of the etch pits was obtained  
109 by multiplying interlayer thickness, 0.4 nm, with the etch pits perimeter. The latter has been  
110 measured using the software ImageJ (Abramoff et al. 2004), with five independent  
111 measurements for each etch pit considered. To our knowledge, no value for the interlayer  $V_m$   
112 has been reported in the scientific literature, therefore it has been approximated as brucite,  
113  $V_m = 24.54 \text{ cm}^3/\text{mol}$  (Rothbaue et al. 1967). Step retreat rate has been evaluated using the  
114 formula  $S = 3\sqrt{3}x^2$ , where  $S$  is the area of an equilateral triangle and  $x$  is the distance between  
115 the center of the triangle and its side. By plotting the  $x$  as a function of time is then possible  
116 to obtain the step retreat rate for each etch pit.

117

### 118 **3. Results**

119 **3.1 Chlorite topography imaged with AFM.** After cleavage, chlorite displays surfaces with  
120 terraces and steps (Fig. 2a). The presence of only one z-level of AFM tapping mode phase  
121 signal data (Fig. 2b) indicates that only one component is exposed, either the interlayer or the  
122 TOT layer. To identify which layer, an area is repetitively scanned for one hour in contact  
123 mode at tip-substrate forces stronger than those normally used for non-invasive imaging. This  
124 process results in the creation of pits which revealed the internal structure of the chlorite (Fig.  
125 2c). Here the exposed layer is about 1 nm thick (line profile), hence this is the TOT layer;  
126 while the second layer, of approximate thickness of 0.4 nm, is the interlayer.

127 Chlorite can also present a discontinuous layer with an irregular appearance and  
128 characteristically constituted by strips and surface gaps when cleaved (Fig. 3), the latter often  
129 with a directionally-oriented triangular shape, as shown in Fig. 3c. Following the convention  
130 of Valdrè et al. (2009), these gaps observed upon cleavage will be referred as “voids”. The  
131 layer thickness of about 4 Å (line profile) indicates that the discontinuous layer is the  
132 interlayer; while the different phase signal of the underlying layer (Fig. 3b) confirms this is  
133 the TOT layer, as expected.

134

135 **3.2 Dissolution of the interlayer in pure water.** Fig. 4a shows an interlayer area after 2  
136 hours immersion in pure water, Fig. 4b shows the same area imaged after a further 2 hours:  
137 comparing these images, it is evident that a dissolution reaction is affecting the interlayer.  
138 The interlayer dissolves via two main pathways: formation of dissolution channels (Figs. 4b,c)  
139 and formation and expansion of mono-oriented equilateral triangular etch pits (Figs.4c-e).  
140 This process lasts for about 3.5 hours and leads to the complete dissolution of the interlayer,  
141 thus exposing the underlying TOT layer, which is not affected by the solution (Figs. 4a-c).  
142 The pH of the dissolution solution was approximately 6 and the morphologies are consistent  
143 with what has been observed in brucite (Kudoh et al. 2006). Here identical triangular etch  
144 pits formed only at neutral or mildly acidic pHs, whereas irregular step retreat has been  
145 observed at lower pH (Jordan and Rammensee 1996; Kudoh et al. 2006).

146

147 The dissolution kinetics was calculated on 5 consecutive AFM images (in the same scan  
148 direction) of an area of 0.2 μm<sup>2</sup> containing 9 expanding etch pits and captured about halfway  
149 of the 3.5 hours-long interlayer dissolution. The dissolution rate was  $6.03 \times 10^{-10} \text{ mol m}^{-2} \text{ s}^{-1}$ ,

7

150 calculated using equation (1) and represented by the gradient of the regression line of Fig. 5a.  
151 Here the moles of dissolved interlayer per square metre are plotted as a function of the time.  
152 Interlayer step retreat rate was calculated for individual etch pit as described in Materials and  
153 Methods (section 2.3), with three examples shown in Fig. 5b. The average value obtained  
154 from all nine etch pits is  $0.0071 \pm 0.0020$  nm/s.

155

156 **3.3 Round-to-triangular etch pit conversion.** Fig. 6 shows the evolution of a set of five  
157 etch pits, recorded within the time interval used for the calculation of the weathering rate  
158 (section 3.2), where three of them expand their triangular shape, while two have an initial  
159 rounded outline (Fig. 6a). Rounded shape has been observed to appear transiently on about  
160 10% of the etch pits in the course of their expanding triangular shape. The expansion process  
161 of the larger rounded etch pit in Fig. 6 involves a preferential enlargement along three faces,  
162 equally spaced on the perimeter by  $120^\circ$ , which results in its conversion into a triangular etch  
163 pit (Figs. 6b,c); a similar process is also present with the smaller rounded etch pit.

164

165 **3.4 Conceptual model: the case of rounded etch pits.** Fig. 7 shows a possible model of  
166 rounded etch pit evolution. Along the etch pit edges, the octahedra arrange in two  
167 configurations easily identifiable as they present either an exposed edge, indicated as “ $\Phi$ ”, or  
168 an exposed corner, indicated as “ $\Psi$ ”. The present model supposes that these configurations  
169 present a different reactivity in water and here we assume that it is the  $\Psi$ -octahedron which is  
170 less stable (see Discussion). As shown in Fig. 7, during dissolution the preferential removal  
171 of  $\Psi$ -octahedra eventually leads to the formation of a triangular etch pit, comparable in  
172 outline shape to the etch pits observed during interlayer dissolution. Etch pit edges are now

8



173 composed of the less-reactive  $\Phi$ -type octahedra. Both experimentally and in the conceptual  
174 model, a preferential dissolution at three equally-spaced areas of the rounded etch pit occurs,  
175 where the putative more highly reactive  $\Psi$ -octahedra are located. Identical results are  
176 obtained when it is assumed that the  $\Phi$ -octahedra are the less stable.

177

178 **3.4 Conceptual model: the case of triangular etch pits.** Only two triangular orientations  
179 are possible on an octahedral layer, which are characterized by different octahedral  
180 configurations along their respective edges:  $\Phi$  for orientation A and  $\Psi$  for orientation B (Fig.  
181 8a). Taking again the  $\Psi$ -configuration as the less stable, the selective removal of  $\Psi$ -octahedra  
182 will convert triangular orientation B to A, Fig. 8b. In contrast the orientation A will continue  
183 to grow maintaining this orientation, as removal of  $\Phi$ -octahedra will expose the same  
184 octahedral configuration. According to the model only one triangular orientation is allowed in  
185 a dissolving octahedral layer and this is indeed what has been observed experimentally, as  
186 shown in Fig. 4e.

187

188

## 189 **4. Discussion**

190 **4.1 Morphology and structure of chlorite imaged with AFM.** Following cleavage, the two  
191 chlorite layers display distinct forms of surface morphology: homogeneous surfaces arranged  
192 in steps and terraces in the case of the TOT layer (Figs. 2a,b), and surfaces pitted with voids  
193 and organized in strips as regards the interlayer component (Fig. 3). The specific pattern of  
194 both layers could result from the cleavage process: in fact, upon removal of the exposed

195 layers with the adhesive tape (see paragraph 2.1), the bonds existing between the stacked  
196 layers could lead to the excision of portions of the newly exposed areas. This is particularly  
197 relevant for the octahedral interlayer, whose lower tensile strength compared to the TOT  
198 tetrahedral layer could lead to the removal of areas in the basal plane, thus determining the  
199 observed voids. However, as it was very difficult to test this hypothesis by imaging the  
200 removed chlorite layers to look for the torn areas, the possibility that the observed features  
201 are pre-existing in the interlayer cannot be ruled out.

202

203 The cleavage origin of interlayer features is supported by other studies (Antognozzi et al.  
204 2006; Valdrè et al. 2009). According to Valdrè et al. (2009), the formation of specific  
205 geometric features in the interlayer after cleavage may be determined by the distribution of  
206 either  $\text{Al}^{3+}$  cations or hydrogen bonds between TOT and interlayer. For example, the highest  
207 density of hydrogen bonds occurs along the [100] direction and could be responsible for the  
208 interlayer strips along the [100] direction, as these are more strongly bound to the underlying  
209 TOT layer. Regarding the triangular voids (Fig. 3c), here we propose that their formation  
210 could be linked instead to the intrinsic octahedral structure of the interlayer. As discussed  
211 later on, triangular etch pits during interlayer dissolution form because this is the most stable  
212 structure the octahedra can assume along the etch pits edge. Therefore it is possible to infer  
213 that during the cleavage, interlayer fragments are removed along the edges of the stable  
214 triangular orientation which hold the interlayer in place, thus leading to triangular voids.

215

216 **4.2 Interlayer dissolution: kinetics.** The  $R^2$  value of 0.997 of the regression line of Fig. 5a  
217 shows that the dissolution rate is linear, which indicates that at this stage, i.e. at about

10

218 halfway of the 3.5 hours-long interlayer dissolution, the varying saturation state over the  
219 course of the experiment is not probably limiting the weathering rate. The latter,  $6.03 \times 10^{-10}$   
220  $\text{mol m}^{-2} \text{s}^{-1}$ , is about two orders of magnitude lower than the rate calculated for brucite with  
221 AFM imaging at pH 5,  $1.10 \times 10^{-8} \text{mol m}^{-2} \text{s}^{-1}$  (Kudoh et al. 2006). This is in line with what  
222 has been observed by Brandt et al. (2003), which reported a rate two orders of magnitude  
223 lower in the interlayer compared to brucite at pH 2. Brandt et al. (2003) attributed this  
224 behaviour to the presence of Fe and Al cations in the interlayer, which reduce the weathering  
225 rate. A similar result is present when the step retreat rate is considered, with a slower rate for  
226 the interlayer ( $0.0071 \pm 0.0020 \text{ nm/s}$ ) compared to brucite,  $0.015 \text{ nm/s}$  (Kudoh et al. 2006).  
227 Similarly to Kudoh et al. (2006), the step retreat has been calculated from the distance centre-  
228 side of ideally perfect equilateral triangular etch pits (see section 2.3). Although the etch pits  
229 often deviate from a perfect equilateral shape, taking the average value for all nine  
230 considered etch pits represents an acceptable approximation of step retreat rate.

231

232 **4.3 Interlayer dissolution: channels.** The presence of dissolution channels in chlorite has  
233 been attributed to mineral structural defects (Brandt et al. 2003), and the channels in the  
234 interlayer may have a similar origin. For example, the main channel of Fig. 4b initially could  
235 have been nucleated following structural defects in the interlayer (its initial formation is  
236 indicated by an arrow in Fig. 4a). The dissolution process can progressively affect and  
237 weaken the nearby areas, where new channels form (Fig. 4b). These structural defects may be  
238 intrinsic to the crystal structure of the mineral flake or could be introduced by the cleaving  
239 procedure, as suggested by the occasional absence of interlayer areas in form of strips and  
240 voids. Channel edges are often observed parallel to the edges of the etch pits, which can

241 coalesce with them, as seen in Fig. 4c. Therefore the same mechanism that leads to the  
242 formation of triangular etch pits, discussed below, can also be involved in the enlargement of  
243 the channels.

244

245 **4.4 Interlayer dissolution: triangular etch pits.** Triangular etch pits form, expand, and  
246 coalesce during dissolution of the chlorite interlayer in pure water (Figs. 4d,e and 6). These  
247 etch pits have an apparent equilateral shape and the same crystallographic orientation, Fig. 4e.  
248 To explain the presence of these peculiar features a conceptual model has been developed, in  
249 which the interlayer was described using the polyhedral representation in CrystalMaker  
250 (CrystalMaker Software Limited, Begbroke, UK), Figs. 7 and 8. In the model, whichever  
251 etch pit shape is created, along their edges the octahedra assume only two distinct  
252 configurations: one with the edge exposed, named here as “ $\Phi$ ”, and the other with an exposed  
253 corner, “ $\Psi$ ” (Fig. 7). After proposing that one octahedral configuration is more prone to  
254 dissolution than the other, this hypothesis was tested by comparing the shapes of dissolving  
255 etch pits in the model with the experimental results. Arbitrarily we considered the  $\Psi$ -  
256 octahedron less stable than the  $\Phi$ -octahedron, although identical conclusions are obtained  
257 when the reactivity order is inverted. In the case of rounded etch pit evolution, both  
258 experimental (Fig. 6) and modeling (Fig. 7) results show that the conversion to the triangular  
259 shape happens through selective dissolution along three equally spaced sections of the  
260 perimeter of the etch pit. In the model, this conversion is due to the preferential dissolution of  
261 the  $\Psi$ -octahedra. These observations show that sites along some crystallographic directions  
262 dissolve faster than others and that triangular etch pits may be the steady state dissolution  
263 feature. Indeed, this is confirmed by the large prevalence of triangular etch pits while the

264 dissolution reaction was at steady state (Fig. 4e), with only few rounded etch pits which  
265 promptly convert in the more stable form (Fig. 6). In addition, while two orientations of  
266 equilateral triangular etch pits are possible on an octahedral layer (Fig. 8a), the etch pits  
267 observed with AFM have the same crystallographic orientation (Fig. 4e). This can be  
268 explained with the conceptual model, in which the triangular orientation with the more  
269 reactive exposed octahedra converts to the more stable orientation during dissolution, as  
270 illustrated in Fig. 8b. More generally, the preferential dissolution of a specific octahedron  
271 (either  $\Psi$ - or  $\Phi$ -) will convert all the possible shapes of etch pits (e.g. squared, rectangular,  
272 and so on) to steady state triangular etch pits that contain the more stable octahedral  
273 configuration along the edges.

274

275 If the origin of the triangular etch pits is indeed crystallographic in nature, this indicates  
276 something about the relative rates of the dissolution reactions that occur on these mineral  
277 surfaces. Materials that grow or dissolve by strongly following crystallographic directions  
278 suggest that the rate of kink site nucleation (removal of the initial material from an otherwise  
279 smooth monomolecular step) is much slower than the rate of kink site propagation (removal  
280 of material neighbouring a previously existing kink) and thus limits the rate of dissolution  
281 (De Yoreo et al., 2009). Materials that grow and dissolve with extremely rough steps likely  
282 contain rates of kink site nucleation and propagation that are similar. This phenomena is most  
283 often discussed with respect to calcite (De Yoreo et al., 2009; Stack and Grantham, 2010), but  
284 other crystalline materials display steps that vary widely in the roughness of their steps,  
285 indicating the density of kinks along the length of the step. The extreme cases are KDP,  
286 where nearly every surface unit cell contains a kink, versus crystalline lysosyme, where one

287 kink is observed every several hundred unit cells (Rashkovich et al., 2006; Rashkovich et al.,  
288 2001). From Figs. 4 and 6, the chlorite interlayer appears to react similarly to calcite (Stack  
289 and Grantham, 2010; Rashkovich et al., 2006) in that some roughness in the steps is observed  
290 but steps still strongly follow crystallographic directions.

291

292 **4.5 Relative stability of triangular etch-pits.** As stated above, there are two possible  
293 crystallographic orientations of the etch pits (Fig. 9). It is not possible to determine uniquely  
294 which of these is dominant from the AFM images alone due to the rotational symmetry of the  
295 crystal. With the exception of the simplest isomorphic materials, this ambiguity is common in  
296 minerals. For some systems such as the calcite {1014} surface, steps such as the acute and  
297 obtuse are aligned with the macroscopic shape of the crystal and so a unique determination  
298 can be made from the orientation of the crystal. Other systems like the barite {001} contain a  
299 screw axis so that the molecular orientation of steps is unknown and the system tends to form  
300 bilayer steps (Higgins et al., 1998). The difficulty in determining the orientation of a given  
301 step on mineral surfaces such as barite and chlorite creates ambiguity in determining precise  
302 molecular level mechanisms; we can tell that one orientation reacts at a different rate, but  
303 inference must be used to determine their identity. For brucite, Kudoh et al. (2006) proposed  
304 that the orientation of the triangular etch pits are consistent with the orientation A of Fig. 9a  
305 by determining the relationship between the triangular etch pits and the crystal structure of  
306 brucite with Electron Back-Scattered Diffraction (EBSD). Again, due to the center of  
307 symmetry, the EBSD cannot distinguish if it is the  $\Psi$ - or  $\Phi$ -octahedra that comprise the etch  
308 pit walls. Kudoh et al. (2006) speculated that the orientation A with the  $\Phi$ -octahedra-  
309 terminated steps is more stable because the OH groups not bound to the underlying TOT

310 layer (OH groups above the plane in Fig. 9a) coordinate with two cations and thus are more  
311 stable than the OH groups in the orientation B with  $\Psi$ -terminated steps, which coordinate to  
312 only one cation (OH groups above the plane in Fig. 9b). The other OH groups present along  
313 the edges in both orientations (OH groups below the plane in Figs. 9a,b) are considered less  
314 reactive as they are bound to the underlying TOT layer via hydrogen bonds.

315

316 Work on the mechanism of oxygen exchange on the alumina  $\epsilon$ -keggin polyoxocations has  
317 revealed an alternate hypothesis. These molecules are composed of sets of three aluminum  
318 octahedra that are bonded in the same arrangements as found in the chlorite interlayer here.  
319 In the proposed mechanism for oxygen exchange of the  $\mu_2$ -oxo species (Rustad et al. 2004), it  
320 was found that the bonds to two of the  $\mu_4$ -oxo groups (i.e., an oxygen shared amongst four  
321 cations) lengthen and dissociate simultaneously, additional water molecules adsorb to  
322 coordinatively saturate the partially-detached octahedra and a metastable intermediate is  
323 formed. Due to their structural similarity, it is reasonable to assume that this reaction pathway  
324 is also present in the brucite-like sheets (including the chlorite interlayer here). In minerals  
325 the metastable intermediate formation may be a precursor to the dissolution of one of both of  
326 the octahedra. This mechanism can help to elucidate the orientation of the etch-pits as well:  
327 the key is that the lengthening of the  $\mu_4$ -oxo bond in the keggin ( $\mu_3$ -hydroxos here) allows the  
328 octahedra to partially detach from the surface. If the  $\Phi$ -octahedra were to lengthen their bond  
329 to the  $\mu_3$ -hydroxo group, it would not lead to a partial detachment of the octahedra because  
330 these are pinned by the hydrogen bonds of their terminal hydroxyls ( $\eta$ -OH) to the TOT layer  
331 below (this species is  $\eta$ -H<sub>2</sub>O in the  $\epsilon$ -keggin). The  $\Psi$ -octahedra also each have a  $\mu_2$ -OH  
332 bound to the TOT layer below, but it is speculated that during the formation of a metastable

333 intermediate, a single species bound to the surface (i.e., the shared  $\mu_3$ -OH) will more readily  
334 act as an axis of rotation, or possibly break its bonds, than the two species bound to the  
335 interlayer below in the  $\Phi$ -octahedra.

336

337 Lastly, the wider rotational axis of the  $\eta$ -OH that are exposed to the solution in the  $\Psi$ -  
338 octahedra will lead to more facile attack by water to coordinate the cation (see Stack et al.  
339 2005 for evidence of this effect on the  $\eta$ -H<sub>2</sub>O groups of the  $\epsilon$ -keggin). In the  $\Phi$ -octahedra, the  
340  $\eta$ -H<sub>2</sub>O may be pinned to the TOT layer below, and the  $\mu_2$ -oxo that are exposed to solution  
341 may have less flexibility, and hence probability of attack by water. Since the etch-pits do  
342 expand over time, it is clear that the  $\Phi$ -octahedra do have a mechanism for detaching  
343 (possibly proton-promoted dissolution at the  $\mu_3$ -OH due to the pH dependence of etch-pit  
344 formation discussed above), but the mechanistic arguments clearly present the hypothesis that  
345 the  $\Psi$ -octahedra will detach more quickly due to this mechanism. Further modeling and  
346 energy calculation studies would be required to test this hypothesis.

347

### 348 **Acknowledgments**

349 This research was undertaken within the framework of the Marie Curie Early Stage Training  
350 project “MISSION”(Mineral Surface Science for Nanotechnology) (MEST-CT-2005-020828)  
351 (SAG, TJM, KVR) and the Center for Nanoscale Control of Geologic CO<sub>2</sub>, an Energy  
352 Frontier Research Center (AGS).

353

### 354 **References**



355 Abramoff, M.D., Magalhaes, P.J., Ram, S.J. (2004) Image Processing with ImageJ.  
356 Biophotonics International, 11, 36-42.

357

358 Aldushin, K., Jordan, G., and Schmahl, W.W. (2006) Basal plane reactivity of phyllosilicates  
359 studied in-situ by hydrothermal atomic force microscopy (HAFM). *Geochimica et*  
360 *Cosmochimica Acta* , 70, 4380–4391.

361

362 Antognozzi, M., Wotherspoon, A., Hayes, J.M., Miles, M.J., Szczelkun, M.D. and Valdrè, G.  
363 (2006) A chlorite mineral surface actively drives the deposition of DNA molecules in  
364 stretched conformations. *Nanotechnology*, 17, 3897-3902.

365

366 Bailey, S.W. (1988) Chlorites: Structures and crystal chemistry. *Review of Mineralogy*, 19,  
367 347-398.

368

369 Bickmore, B.R., Bosbach, D., Hochella, M.F., Charlet, L. and Rufe, E. (2001) In situ atomic  
370 force microscopy study of hectorite and nontronite dissolution: Implications for phyllosilicate  
371 edge surface structures and dissolution mechanisms. *American Mineralogist*, 86, 411-423.

372

373 Binnig, G., Quate, C.F. and Gerber, C. (1986) Atomic Force Microscope. *Physical Review*  
374 *Letters*, 56, 930-933.

375

376 Brandt, F., Bosbach, D., Krawczyk-Barsch, E., Arnold, T. and Bernhard, G. (2003) Chlorite  
377 dissolution in the acid pH-range: A combined microscopic and macroscopic approach.  
378 *Geochimica Et Cosmochimica Acta*, 67, 1451-1461.

379

380 De Yoreo, J.J., Zepeda-Ruiz, L. A., Friddle, R. W., Gilmer, G. H., Chernov, A. A. and Dove,  
381 P.M. (2009) Rethinking classical crystal growth models through molecular scale insights:  
382 Consequences of kink-limited kinetics. *Crystal Growth and Design*, 9, 5135–5144.

383

384 Hamer, M., Graham, R. C., Amrhein, C. and Bozhilov, K. N. (2003) Dissolution of ripidolite  
385 (Mg, Fe-chlorite) in organic and inorganic acid solutions. *Soil Science Society of America*  
386 *Journal*, 67, 654-661.

387

388 Higgins S. R., Jordan G, Eggleston C. M. and Knauss K. G. (1998) Dissolution kinetics of  
389 the barium sulfate (001) surface by hydrothermal atomic force microscopy. *Langmuir*, 14,  
390 4967-4971.

391

392 Horcas, I., Fernandez, R., Gomez-Rodriguez, J.M., Colchero, J., Gomez-Herrero, J. and Baro,  
393 A.M. (2007) WSXM: A software for scanning probe microscopy and a tool for  
394 nanotechnology. *Review of Scientific Instruments*, 78, 013705.

395

396 Jordan, G. and Rammensee, W. (1996) Dissolution rates and activation energy for dissolution  
397 of brucite (001): A new method based on the microtopography of crystal surfaces.  
398 *Geochimica Et Cosmochimica Acta*, 60, 5055-5062.

399 .

400 Glowa, K.R., Arocena, J.M. and Massicotte, H.B. (2003) Extraction of potassium and/or  
401 magnesium from selected soil minerals by *Piloderma*. *Geomicrobiology Journal*, 20, 99-111.

402

403 Kudoh, Y., Kameda, J. and Kogure, T. (2006) Dissolution of brucite on the (001) surface at  
404 neutral pH: In situ atomic force microscopy observations. *Clays and Clay Minerals*, 54, 598-  
405 604.

406

407 Kuwahara, Y. (2001) Comparison of the surface structure of the tetrahedral sheets of  
408 muscovite and phlogopite by AFM. *Physics and Chemistry of Minerals*, 28, 1–8.

409

410 Maurice, P.A. (1996). Applications of atomic-force microscopy in environmental colloid and  
411 surface chemistry. *Colloids and Surfaces A: Physicochemical and Engineering Aspects*, 107,  
412 57-75.

413

414 Rashkovich L. N., De Yoreo J. J., Orme C. A. and Chernov A. A. (2006) In situ atomic force  
415 microscopy of layer-by-layer crystal growth and key growth concepts. *Crystallography*  
416 *Reports*, 51, 1063–1074.

417

418 Rashkovich L. N., Gvozdev N. V., Silnikova M. I., Yaminski I. V. and Chernov A. A. (2001)  
419 Dependence of the step velocity on its length on the (0 1 0) face of the orthorhombic  
420 lysozyme crystal. *Crystallography Reports*, 46, 860.

421

422 Rothbaue, R., Zigan, F., Odaniel, H. (1967) Refinement of Structure of Bayerite  $\text{Al}(\text{OH})_3$ .  
423 Including a suggestion for H position. *Zeitschrift Fur Kristallographie Kristallgeometrie*  
424 *Kristallphysik Kristallchemie*, 125, 317.

425

426 Rufe, E. and Hochella, M.F. (1999) Quantitative assessment of reactive surface area of  
427 phlogopite during acid dissolution. *Science*, 285, 874-876.

428

429 Rustad, J.R., Loring, J.S., Casey, W.H. (2004) Oxygen-exchange pathways in aluminum  
430 polyoxocations. *Geochimica et Cosmochimica Acta*, 68, 3011-3017.

431

432 Sánchez-Pastor, N., Aldushin, K., Jordan, G., Schmahl, W.W. (2010)  $\text{K}^+$ - $\text{Na}^+$  exchange in  
433 phlogopite on the scale of a single layer. *Geochimica et Cosmochimica Acta*, 74, 1954-1962.

434

435 Schmitz, I., Schreiner, M., Friedbacher, G. and Grasserbauer, M. (1997) Phase imaging as an  
436 extension to tapping mode AFM for the identification of material properties on humidity-  
437 sensitive surfaces. *Applied Surface Science*, 115, 190-198.

438

439 Stack, A. G. and Grantham, M. C. (2010) The growth rate of calcite steps as a function of  
440 aqueous calcium-to-carbonate ratio: independent attachment and detachment of calcium and  
441 carbonate ions. *Crystal Growth and Design*, 10, 1409-1413.

442

443 Stack, A.G., Rustad, J.R., and Casey, W.H. (2005) Modeling water exchange on an aluminum  
444 polyoxocation. *Journal of Physical Chemistry B*, 109, 23771-23775.

445

446 Valdrè, G., Malferrari, D. and Brigatti, M.F. (2009) Crystallographic features and cleavage  
447 nanomorphology of chlinochlore: specific applications. *Clays and Clay Minerals*, 57, 183-  
448 193.

449

450 White, A.F. and Brantley, S.L. (1995) *Chemical Weathering Rates of Silicate Minerals*,  
451 Mineralogical Society of America.

452

453

## 454 **Figures**

455 **Figure 1.** Schematic structure of chlorite. The tetrahedral sheets, light blue in colour, contain  
456  $\text{Si}^{4+}$  and  $\text{Al}^{3+}$  cations in the ratio 3:1, and the octahedral sheets, yellow in colour, contain  
457  $\text{Mg}^{2+}$ ,  $\text{Fe}^{2+/3+}$  and  $\text{Al}^{3+}$  cations. The interlayer is sandwiched between two TOT layers through  
458 hydrogen bonds. The thickness of chlorite unit cell, composed of a TOT layer and the  
459 interlayer, is 14 Å (Bailey, 1988), where the TOT has a thickness of 10 Å and the interlayer  
460 of 4 Å. Image generated using CrystalMaker® v. 2.3.

461

462 **Figure 2.** TOT-exposed chlorite. In some areas the solvent-exposed surface of chlorite (a)  
463 displays a single composition as revealed by the presence of only one phase signal level (b).  
464 Chlorite etch pits, derived from continuous and invasive scanning of the surface in contact  
465 mode, are shown in (c). Within the etch-pit a second underlying layer, partially exposed by  
466 the scanning, is visible. The depth of the solvent-exposed layer is 10 Å (line profile) and  
467 corresponds to the TOT layer. The depth of the underlying layer is 4 Å and corresponds to the  
468 interlayer. Z range: 0-12 nm (a), 0-15° (b), 0-2.6 nm (c).

469

470 **Figure 3.** Interlayer can present strips and areas with voids (a). The identity of the interlayer  
471 is confirmed by its thickness ( $\sim 4$  Å, line profile) and the difference in the phase signal data  
472 from the underlying TOT layer (b). The peaks present in the line profile corresponds to the  
473 impurities on the interlayer, shown as rounded white particles in (a). Voids can also have an  
474 equilateral triangular shape with the same spatial orientation (asterisks in c). Z range: 0-3 nm  
475 (a,c), 0-20° (b).

476

477 **Figure 4.** The interlayer surface dissolves through dissolution channels (b,c) and etch pits  
478 (c,d,e). Following two hours in contact with water, the initial formation of the main channel  
479 is indicated by an arrow in (a). After further two hours, channels extend in the interlayer  
480 surface (b,c). In (c) a higher magnification of a channel segment is displayed, where the  
481 asterisk indicates an etch pit that is coalescing with the channel. Channel edges are parallel to  
482 etch pits edges, which have a mono-oriented triangular shape (c,d,e). The area in (a) has been

483 captured about halfway of the overall dissolution reaction. Some of the expanding etch pits  
484 are indicated by numbers in (d) and (e). Z ranges: 0-10 nm (a,b), 0-2 nm (c), 0-5 nm (d,e).

485

486 **Figure 5.** In (a) a dissolving area of  $0.2 \mu\text{m}^2$ , containing nine etch pits, is plotted in function  
487 of the time. The standard deviation for each point is indicated by error bars in the plot and  
488 their values range between  $0.037 \times 10^{-7} \text{ mol/m}^2$  and  $0.244 \times 10^{-7} \text{ mol/m}^2$ : for their low value,  
489 the errors bars are often graphically masked by the respective points. The dissolution rate,  
490 obtained from the slope of the regression line, is  $6.03 \times 10^{-10} \text{ mol m}^{-2} \text{ s}^{-1}$ . The  $R^2$  value of the  
491 regression line is 0.997. In (b) the distance between the center of equilateral triangular etch  
492 pits and their side is plotted in function of the time. The step retreat for three etch pits is  
493 displayed, with step retreat rates of 0.0079 nm/s (squares), 0.0058 nm/s (rhombi) and 0.0060  
494 nm/s (triangles).

495

496 **Figure 6.** Etch pits evolution in a time interval of 13 min, captured midway of the dissolution  
497 process. Three equilateral triangular etch pits are present in (a), which expands and coalesce  
498 maintaining the triangular shape (b, c). Two initially rounded shaped etch pits (a) convert to a  
499 triangular form (b,c) through a preferential expansion along three equidistant regions,  
500 indicated by arrows in (a) and (c). Z range: 0-5 nm (a,b), 0-6 nm (c).

501

502 **Figure 7.** Modeling of the evolution of a rounded etch pit. The edges of the etch pit presents  
503 either corner-exposed octahedra ( $\Psi$  configuration) or edge-exposed octahedra ( $\Phi$   
504 configuration) (a). The higher reactivity of the  $\Psi$  configuration expose more  $\Phi$  octahedra (b)

505 and eventually leads to the formation of an equilateral triangular etch pit with only  $\Phi$   
506 octahedra exposed to the solution. Images generated using CrystalMaker® v.2.3.

507

508 **Figure 8.** Relative stability of triangular etch pits on an octahedral layer. (a) Two different  
509 orientations (indicated as A and B) can be originated on an octahedral layer, with each one  
510 presenting edges with either edge-exposed octahedra ( $\Phi$  octahedra in orientation A) or  
511 corner-exposed octahedra ( $\Psi$  octahedra in orientation B). (b) The preferential dissolution of  
512 the  $\Psi$  octahedra leads to the conversion from orientation B to orientation A, which edges  
513 present only  $\Phi$  octahedra. Broken lines represent the region previously occupied by the  
514 removed octahedra. Images generated using CrystalMaker® v. 2.3.

515

516 **Figure 9.** Polyhedral (right) and ball-and-stick (left) representations of the two triangular  
517 orientations possible on an octahedral layer. In the ball-and-stick representation, the plane  
518 defined by the cation atoms (yellow) is shown in gray. The OH groups (orange) below the  
519 plane are darker in colour and are bound to the underlying TOT layer through H-bonds.  
520 Examples of  $\eta$ -OH,  $\mu_2$ -OH and  $\mu_3$ -OH groups are shown. The  $\Psi$ -terminated step (Orientation  
521 B) is likely less stable because the mechanism of dissolution is more facile. Images generated  
522 using CrystalMaker® v.2.3.



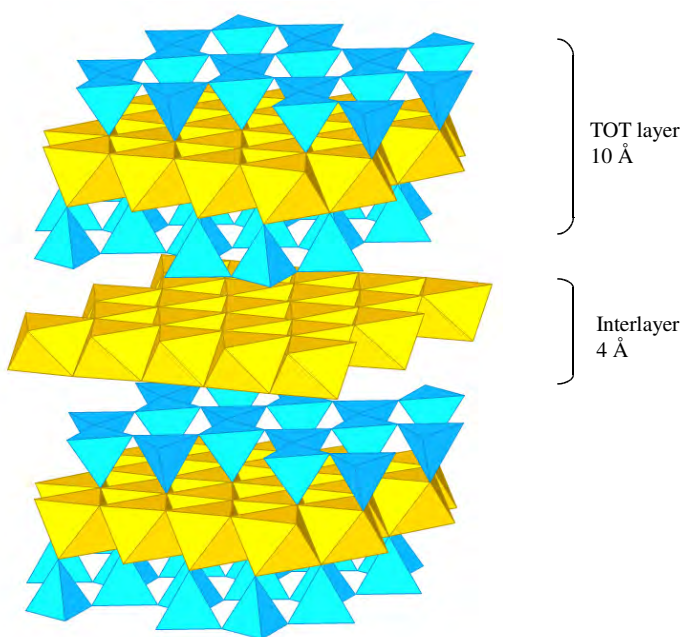


**Figure 1.**

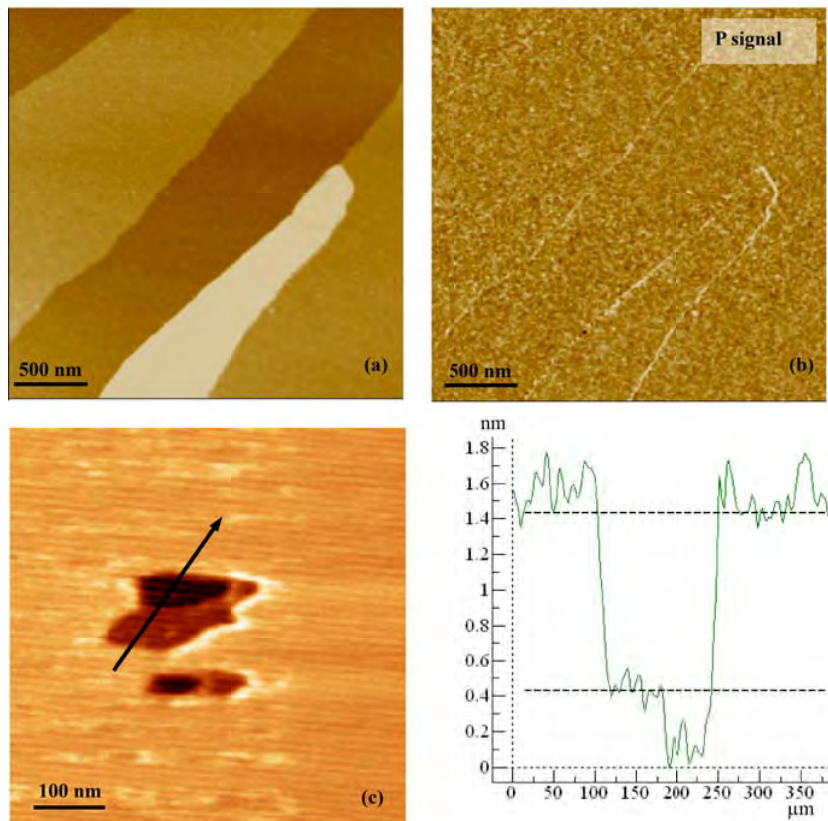


Figure 2.

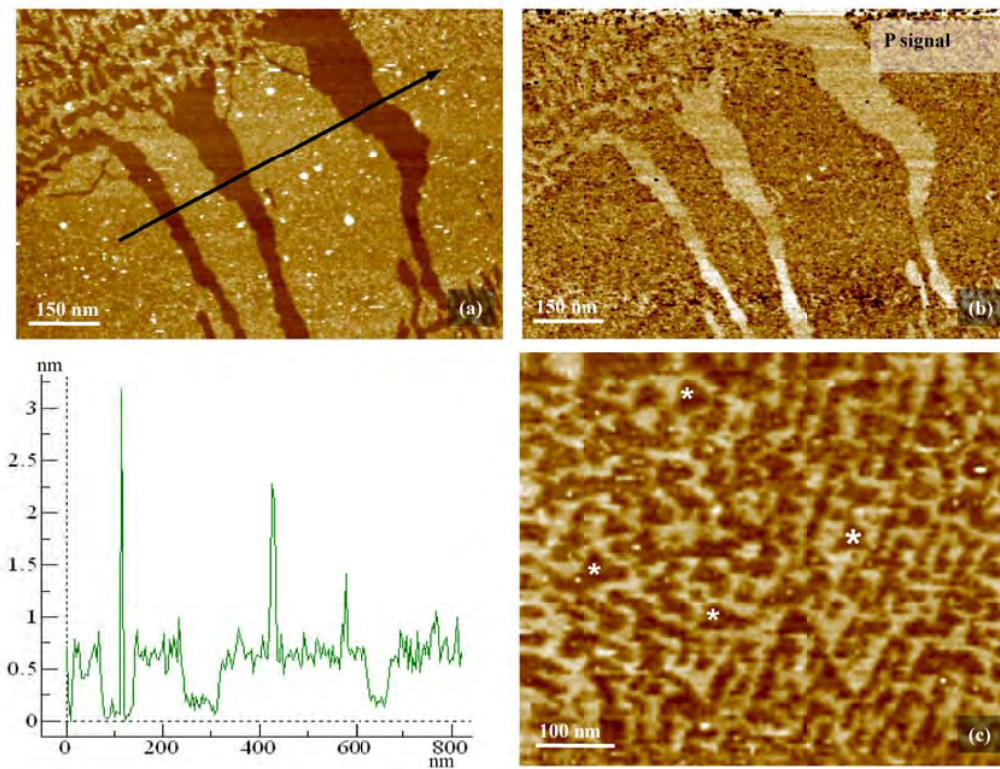


Figure 3.

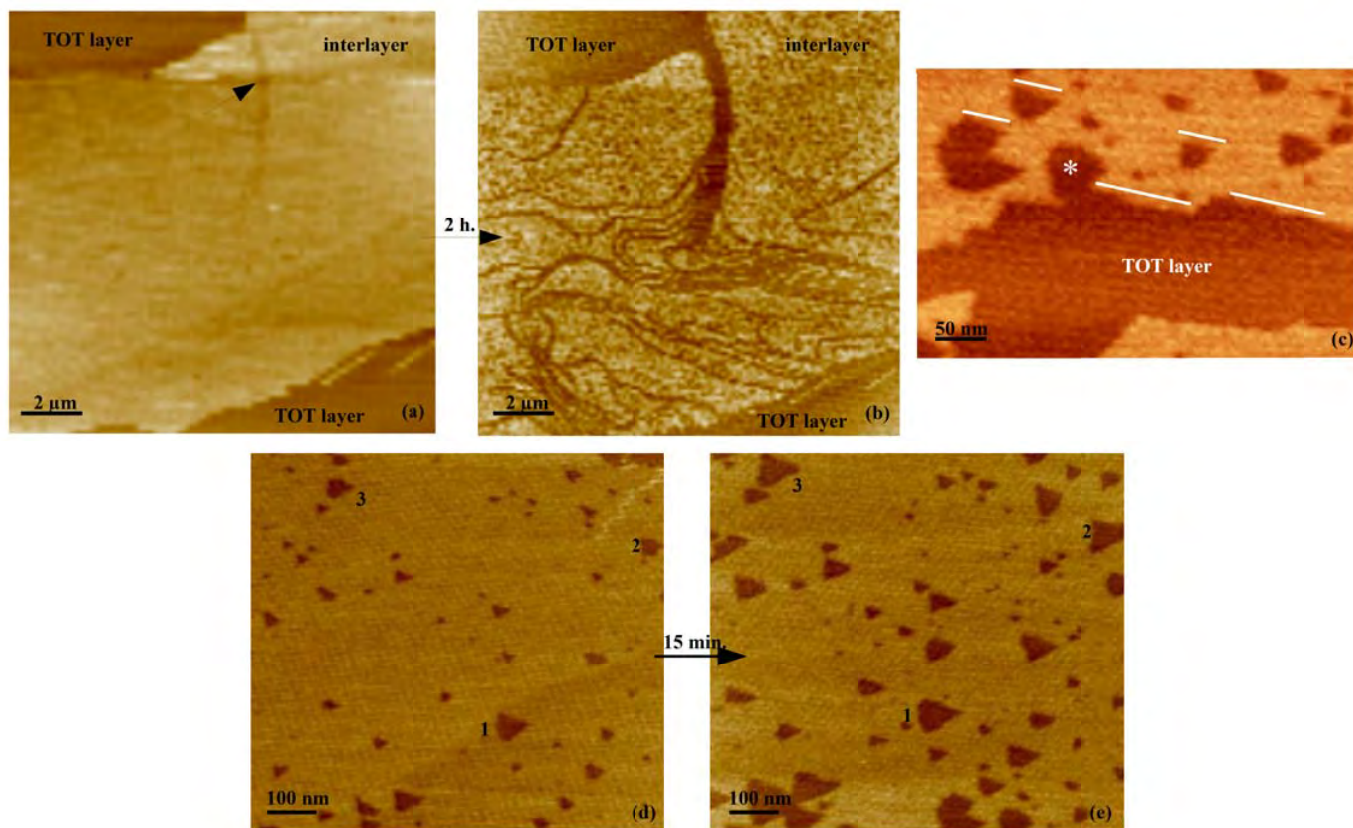


Figure 4.

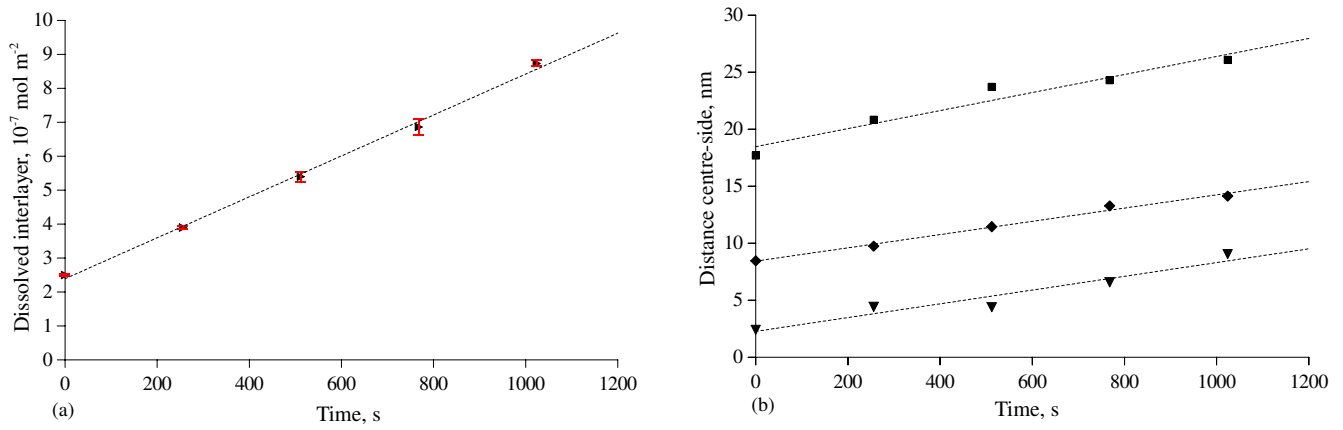
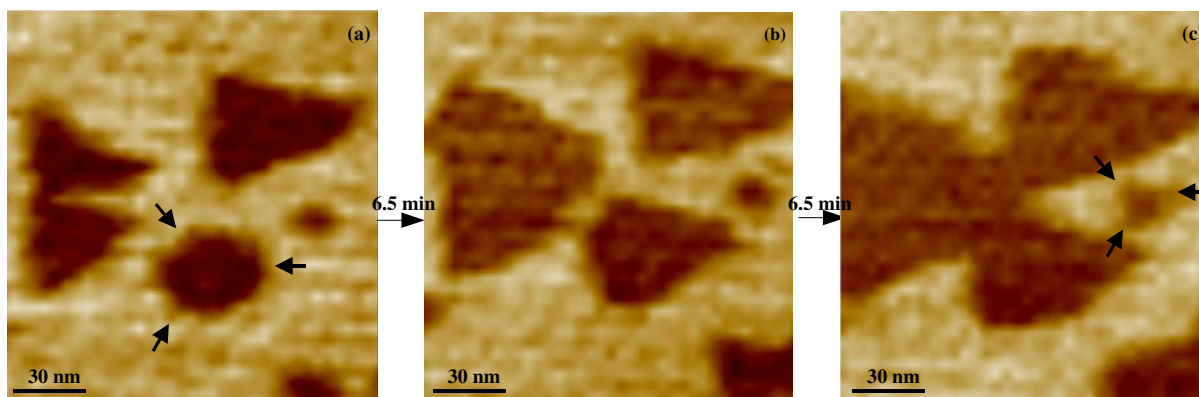


Figure 5.





**Figure 6.**

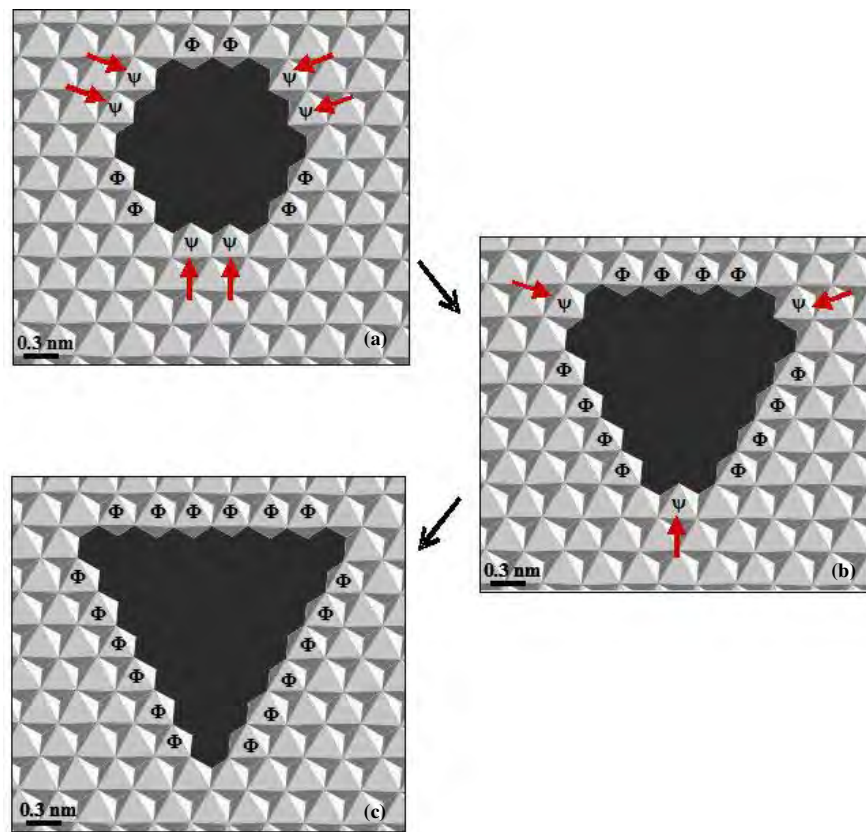


Figure 7.

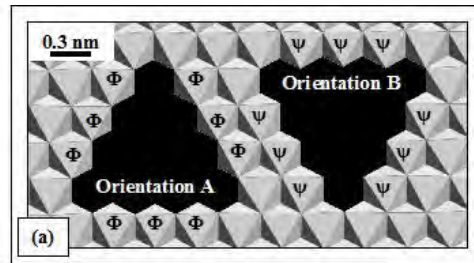
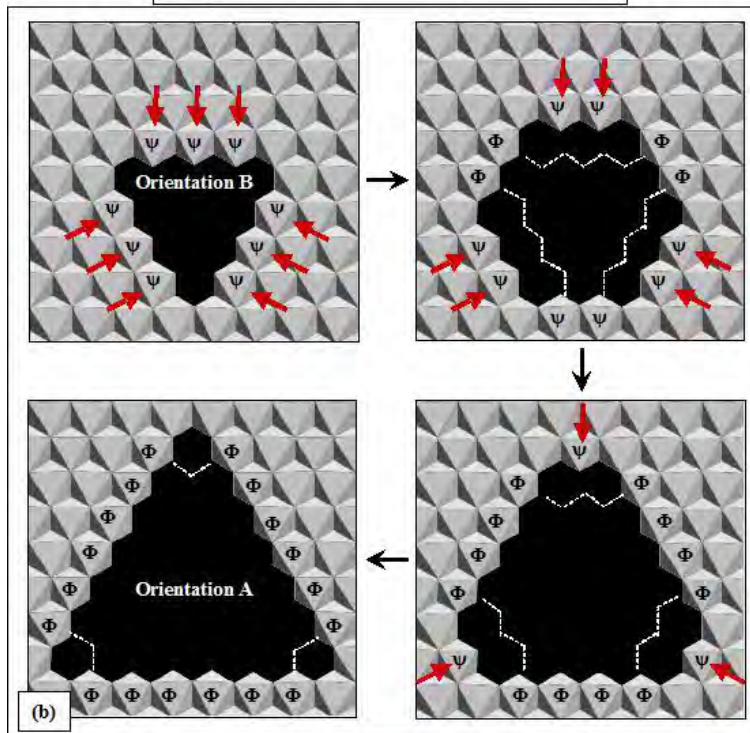


Figure 8.





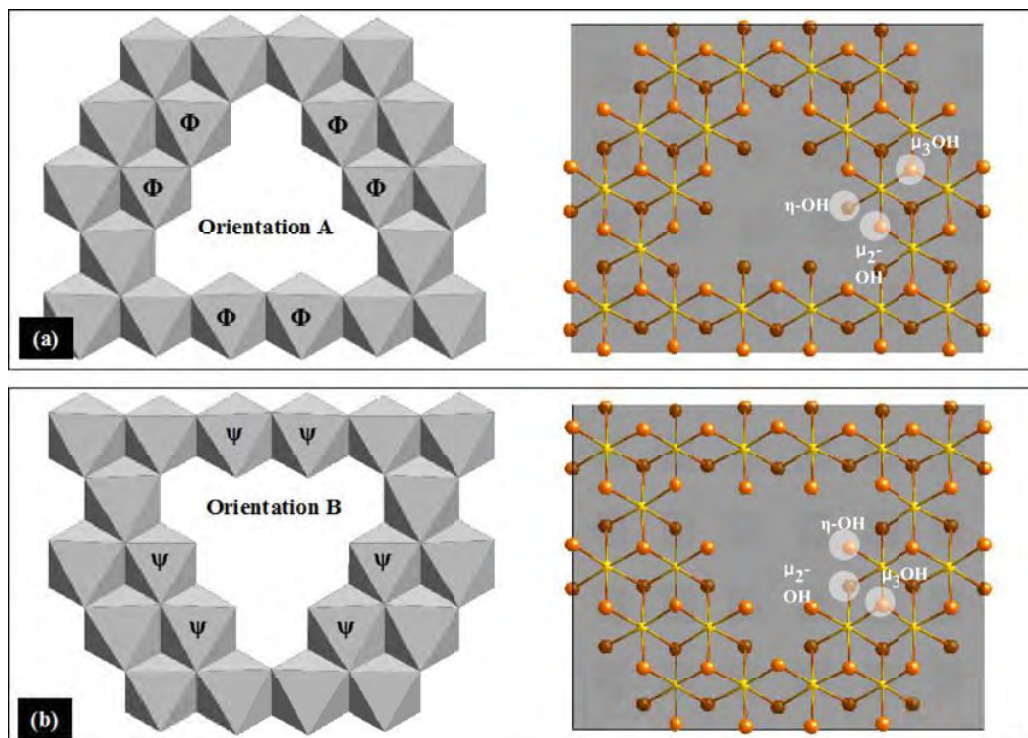


Figure 9.